THE JOURNAL OF PHYSICAL CHEMISTRY C

Article

pubs.acs.org/JPCC

$ZnFe_2O_4$ Nanotubes: Microstructure and Magnetic Properties

Xuan Guo,[†] Haojun Zhu,[†] Mingsu Si,[‡] Changjun Jiang,[‡] Desheng Xue,[‡] Zhihua Zhang,[§] and Quan Li*[,†]

[†]Department of Physics, The Chinese University of Hong Kong, Shatin, New Territories, Hong Kong

[‡]Key Laboratory for Magnetism and Magnetic Materials of the Ministry of Education, Lanzhou University, Lanzhou, 730000, People's Republic of China

[§]School of Materials Science and Engineering, Dalian Jiaotong University, Dalian 116028, People's Republic of China

ABSTRACT: Employing an electron energy-loss spectrum (EELS), we have found that the structure of $ZnFe_2O_4$ nanotubes deviated from the normal spinel structure as the calcination temperature decreases. More Fe^{3+} ions migrate to the tetrahedral sites (A sites) rather than staying in their equilibrium octahedral sites (B sites). This results in the enhanced superexchange interactions between Fe^{3+} ions, thus affecting the magnetic properties of the nanotubes, i.e., higher blocking temperature (T_B) and larger saturation magnetization (M_S), etc. On the other hand, we have also found that deviation of the Fe/Zn from 2 affects the magnetic properties of the nanotube samples. This should be caused by the enhanced superexchange interactions resulting from the extra Fe^{3+} ions in the nonstoichiometric sample.

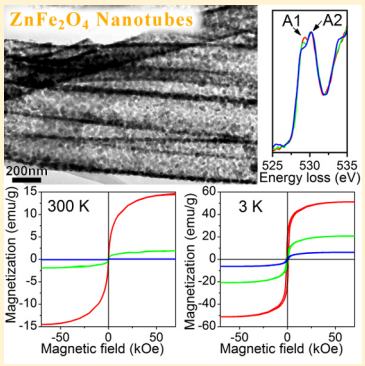

INTRODUCTION

Bulk zinc ferrite ($ZnFe_2O_4$) has a normal spinel structure. Each unit cell of $ZnFe_2O_4$ contains 56 ions, including 32 oxygen anions, 8 zinc cations, and 16 ferric cations. All of the oxygen anions are arranged in a close-packed face-centered cubic (fcc) lattice, leading to the formation of two kinds of interstitial sites in the lattice, i.e., 64 tetrahedral sites (A sites) and 32 octahedral sites (B sites). In the normal spinel structure of $ZnFe_2O_4$, one-eighth of the A sites are filled with Zn^{2+} cations and half of the B sites are filled with Fe^{3+} cations.[1] However, in some cases, the divalent cations (e.g., Zn^{2+}) probably transfer from their equilibrium positions (A sites) to the B sites, while the trivalent cations (e.g., Fe^{3+}) transfer in a reverse manner (from B sites to A sites). The cation inversion is commonly observed in nanocrystalline $ZnFe_2O_4$[2−17] and is typically described using cation inversion degree δ ($0 \le \delta \le 1$). Using this parameter, the site occupation of $ZnFe_2O_4$ can be denoted by a general formula $(Zn_{1-\delta}Fe_{\delta})[Zn_{\delta}Fe_{2-\delta}]O_4$, where the round and the square brackets give the elements in A and B sites, respectively. The change in atomic arrangement of the cations in zinc ferrites affect both its structural characteristics and physical properties that are sensitive to the crystalline structure, such as its magnetic behavior.[2,4−7,9,13,15,17−19]

Consequently, characterization of the microstructure of the nanocrystalline $ZnFe_2O_4$, in particular, the local coordination environment of its cations, is extremely important in understanding the material's physical properties. Several characterization techniques have been used to disclose the local coordination environment of $ZnFe_2O_4$, including neutron diffraction,[8,9,19] X-ray absorption fine structures,[13−16,18] and Mössbauer spectroscopy.[2−6,8,10−12,17] Hofmann et al. deducted the cation inversion degrees of a series of nanostructured $ZnFe_2O_4$ samples synthesized by milling from their neutron diffraction results.[9] Nakashima et al. estimated the cation inversion degrees of several sputtered $ZnFe_2O_4$ thin film using the X-ray absorption near-edge structures (XANES) with the help of theoretical calculations.[13] Li et al. also estimated the cation inversion degree of $ZnFe_2O_4$ nanoparticles from their Mössbauer spectra at 4.2 K.[10] However, these techniques are all macroscopic and disclose averaged structure information on the nanocrystalline $ZnFe_2O_4$. On the other hand, the spatial resolution of the energy-loss near-edge structure (ELNES) techniques in a TEM are down to subnanometer scale, which provides an excellent means to study nanomaterials. ELNES is very sensitive to the change of the local coordination environment of its compositional elements. Such a technique can be used to detect the Fe^{3+} ions distribution in the spinel structure. Indeed, Colliex et al.[20] studied O K edges of several different iron oxides, including spinel Fe_3O_4 (half of Fe^{3+} in O^{2-} octahedron), spinel γ-Fe_2O_3 (half of Fe^{3+} in O^{2-} octahedron), and rhombohedral α-Fe_2O_3 (all of Fe^{3+} in O^{2-} octahedron). They found out that the peak near 532 eV splits into two components, and their separation and ratios are different for the iron oxides with different symmetry of O^{2-} ions surrounding Fe^{3+}. Nevertheless, the ELNES study of $ZnFe_2O_4$ is not available to date.

In the present work, we have employed EELS to investigate the local coordination environment of the cations in both calcination-temperature-dependent and chemical-composition-dependent $ZnFe_2O_4$ sample series. In these samples, we have

Received: August 7, 2014
Revised: October 31, 2014
Published: November 25, 2014

measured the samples' magnetic properties as functions of both the processing temperature and chemical composition. The correlation between the magnetic properties and the specific microstructure (obtained by ELNES study)/chemical composition of the $ZnFe_2O_4$ nanotube samples is discussed in detail.

EXPERIMENTAL SECTION

The $ZnFe_2O_4$ nanotubes were synthesized using ZnO nanowire arrays as the sacrificial template via the similar procedures as described elsewhere.[21] Briefly, ZnO nanowire arrays were first prepared on the seeded sapphire substrates (50.8 mm in diameter) by the hydrothermal method at 95 °C using 25 mM $Zn(CH_3COO)_2{\cdot}2H_2O$ and 25 mM hexamethylenetetramine (HMT) solution in a 250 mL Teflon container. The solution was renewed every 4 h, and the total synthesis took 16 h. Next, two series of samples (i.e., the temperature series and the stoichiometric series) were fabricated using different synthetic parameters. For the temperature series, the obtained ZnO nanowire arrays were immersed into 0.05 M $FeCl_3$ aqueous solution with vigorous shaking for 10 s. Then the samples were calcined in the air for 5 h at 400, 500, and 600 °C, respectively. This leaded to the formation of the $ZnO/ZnFe_2O_4$ nanocable arrays on the substrates. Then the excess ZnO cores in all the samples after calcination was completely removed by 1% HCl solution for 0.5 h, forming tubular morphology. These three samples were labeled as S400, S500, and S600. For the stoichiometric series, the $FeCl_3$ immersion time of ZnO templates increased from 10 to 20 s, so that more iron compounds were coated on the ZnO surface and more nanowire templates were consumed. The amount of iron compounds became excessive to form stoichiometric $ZnFe_2O_4$ after 5 h calcinations at 500 °C. Thus, Fe:Zn ratios in the final nanocables were larger than 2. A similar etching process was performed in order to get rid of the ZnO core and generate the nanocable morphology. This sample was labeled as S500NS. Finally, the nanotubes were washed for several times by DI water and ethanol using centrifugation and dried for further characterizations.

The crystallinity of the $ZnFe_2O_4$ samples was examined by X-ray diffraction (XRD) using a diffractometer with Cu Kα radiation (Rigaku SMARTLAB XRD). Raman spectra were recorded with a Raman spectrometer (Renishaw RM1000B) equipped with an optical microscope (Leica). The excitation source was a 514.5 nm argon ion laser (Spectra-Physics). The chemical states of each element in the samples were studied by X-ray photoelectron spectra (XPS, ThermoFisher ESCALAB 250) using Al Kα radiation ($h\nu$ = 1486.6 eV). All the recorded binding energies (BE) were calibrated by using the C 1s peak (BE = 284.8 eV) from absorbed hydrocarbon as a reference. The microstructures were characterized by transmission electron microscopy (TEM; Tecnai G2 FEG). EELS of the samples were collected using the Gatan FS1 system attached to another TEM (Tecnai 20 ST), with an energy resolution of ~0.7 eV and signal-to-noise ratio on the order of 100. The rapidly decreasing background of O K edge raw data are fitted and then subtracted using the standard exponential fitting model. Then, the background of the peak near 530 eV is fitted using a polynomial function, and the two peak components are fitted using Voigt functions. There are two main mechanisms for the broadening of these peaks. One is due to energy broadening of the incident beam and other instrumental/random statistical effects. This makes the peaks having a Gaussian profile. The other can be attributed to the natural width of the initial and final energy states of the electron transitions. This makes the peaks having a Lorentzian profile. Convolution of a Gaussian and a Lorentzian function gives the Voigt profile, which is commonly adopted in the literature.[22] The selective-area electron diffraction (SAD) patterns were taken on another TEM (Tecnai Spirit 12). The zero-field-cooling (ZFC) and field-cooling (FC) curves and magnetic hysteresis loops (at 3 and 300 K) were recorded using a superconducting quantum interference device (SQUID) magnetometer MPMS XL-7 from Quantum Design Inc. with the maximum external magnetic fields of 70 000 Oe.

RESULTS AND DISCUSSION

Common Structural Characteristics of All $ZnFe_2O_4$ Nanotubes. The crystalline structures of the $ZnFe_2O_4$ nanotube samples were first investigated by XRD. All samples show similar XRD results, and a representative XRD spectrum taken from the nanotube sample S600 is shown in Figure 1a.

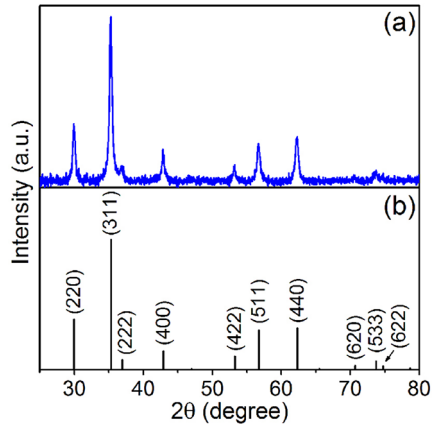

Figure 1. (a) Representative XRD spectrum of $ZnFe_2O_4$ nanotubes (sample S600) and (b) the standard XRD data of $ZnFe_2O_4$ (JCPDS No. 89-7412).

Comparing to the standard diffraction data of $ZnFe_2O_4$ (JCPDS No. 89-7412) in Figure 1b, all peaks can be indexed to its cubic spinel structure. No other diffraction peak is detected. The average crystalline sizes of these samples can be estimated using Scherrer's equation, and the average grain sizes estimated from the full width at half-maximum (fwhm) of the (311) diffraction peaks of the four samples are similar, ranging from 23 to 28 nm, as summarized in Table 1.

Table 1. Average Grain Sizes of Samples S400, S500, S600, and S500NS

sample	2θ (deg)	fwhm (deg)	av grain size (nm)
S400	35.30	0.44	~23
S500	35.30	0.41	~25
S600	35.34	0.37	~28
S500NS	35.28	0.40	~26

It is important to note that some phases of iron oxides, including the magnetite (Fe_3O_4) and maghemite (γ-Fe_2O_3), also have the cubic spinel structure. Their lattice parameters are slightly smaller than that of $ZnFe_2O_4$. However, the difference in the lattice parameters is too small (i.e., 0.8422 nm for $ZnFe_2O_4$, 0.8396 nm for Fe_3O_4, and 0.8352 nm for γ-Fe_2O_3) to be distinguished from the present XRD data.

dx.doi.org/10.1021/jp507991e | J. Phys. Chem. C 2014, 118, 30145−30152

In order to confirm the phase of $ZnFe_2O_4$ (instead of a mixture with various iron oxide phases), Raman spectroscopy was carried out on the respective samples. The Raman spectra taken from all $ZnFe_2O_4$ samples show similar features, and a representative Raman spectrum (sample S600) is shown in Figure 2. Two peaks around 347 and 660 cm^{-1} are observed,

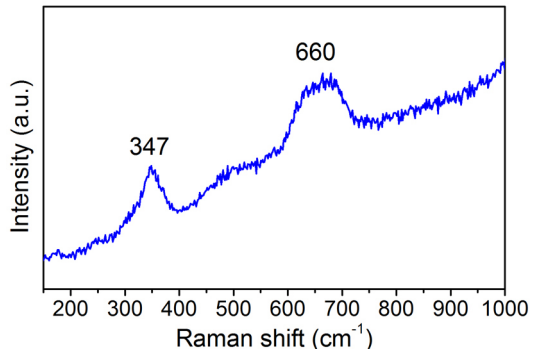

Figure 2. Representative Raman spectrum of $ZnFe_2O_4$ nanotubes (sample S600).

being consistent with the literature-reported values of phase pure $ZnFe_2O_4$.[23,24] No fingerprint peak of the iron oxide phase, including both γ-Fe_2O_3 and Fe_3O_4, is identified.

Detailed microstructure analyses of the four samples were performed using TEM-related techniques. All samples present hollow tubular morphology with the inner diameters 150−200 nm and wall thicknesses ~30 nm, as shown in Figure 3a. The corresponding magnified TEM images (Figure 3b) show the crystalline sizes of $ZnFe_2O_4$ are around 20−30 nm, which are consistent with the XRD results. Selected area diffraction (SAD) patterns taken from all four samples (Figure 3c) also exhibit similar ring patterns, suggesting the polycrystalline nature of the nanotubes. All of these rings can be indexed to spinel structures, which is also consistent with the XRD data.

The chemical composition and the electronic structure of individual nanotubes were investigated using EELS. A representative core-loss spectrum of $ZnFe_2O_4$ nanotubes (S600), recorded from 450 to 1450 eV, is shown in Figure 4a. The presence of O K edge, Fe L edge, and Zn L edge indicates the sample composition of O, Fe, and Zn. The fine structures of Fe L edge was collected at higher energy resolution (Figure 4b), showing two main peaks (i.e., L_3 and L_2), which correspond to the electron excitations from the spin−orbit splitting levels $2p_{3/2}$ and $2p_{1/2}$ to the empty density of states in the material conduction band.[20,25] Moreover, both

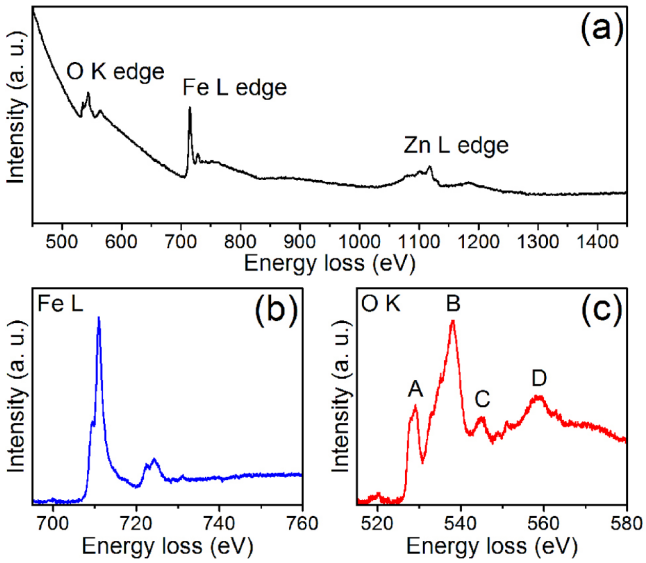

Figure 4. (a) A typical full core-loss spectrum, (b) Fe L edge, and (c) O K edge spectra after background subtraction for $ZnFe_2O_4$ nanotube sample S600.

the L_3 and L_2 peaks are further split into two peaks, due to the p−d Coulomb and exchange interactions.[20] The ELNES of O K edge is more complex and consists of four main peaks, labeled as A, B, C, and D, respectively (shown in Figure 4c). Peaks A and B originate from electron transitions from O 1s to the unoccupied states in the O 2p orbitals hybridized with Fe 3d orbitals, and to higher-energy orbitals composed mainly of 4sp levels of Zn and Fe, respectively. Peaks C and D come from the electron backscattering of the nearest and second-nearest coordination shells around ionized O atoms, respectively.[20]

Calcination-Temperature Effect on $ZnFe_2O_4$ Nanotubes. *Chemical Composition of the Stoichiometric $ZnFe_2O_4$ Nanotubes.* The chemical compositions of the $ZnFe_2O_4$ nanotube samples and the chemical states of the compositional elements (i.e., Zn, Fe, and O) were examined using XPS. All samples in this series show similar XPS results. Figure 5 shows a representative XPS spectrum of the calcination temperature dependent sample series (i.e., S400, S500, and S600, and the presented data are taken from S400). The survey scan (Figure 5a) shows that the sample consists of Zn, Fe, and O only. (The C signal comes from the adsorbed hydrocarbon.) The fine scan of Zn 2p (Figure 5b) shows two peaks at 1021.6 and 1044.7 eV, which can be attributed to Zn $2p_{3/2}$ and Zn $2p_{1/2}$, respectively. It indicates that the oxidation state of Zn is +2 in the

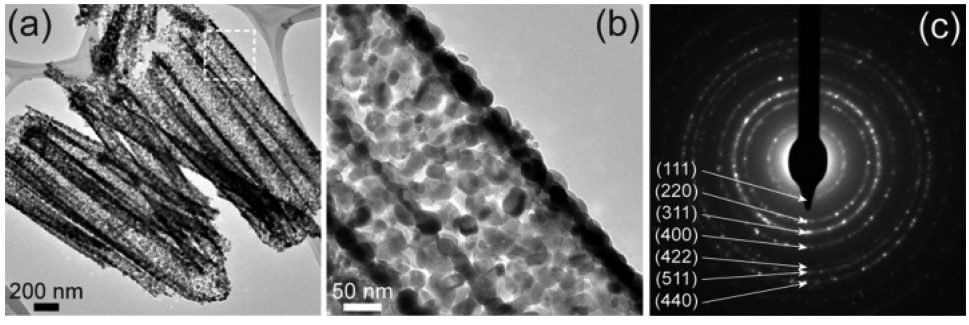

Figure 3. (a) Representative low-magnification TEM image of $ZnFe_2O_4$ nanotube samples. (b) Magnified TEM image of the area marked by the dashed box in (a). (c) Corresponding SAD pattern.

dx.doi.org/10.1021/jp507991e | J. Phys. Chem. C 2014, 118, 30145−30152

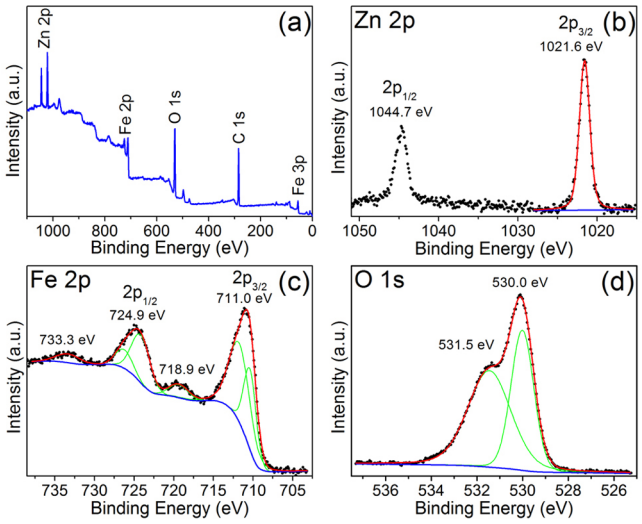

Figure 5. Representative XPS spectra of (a) survey scan and fine scans (black dots) of (b) Zn 2p, (c) Fe 2p, and (d) O 1s taken from stoichiometric $ZnFe_2O_4$ nanotube sample S400. In panels b–d, the blue line is the fitted background using Shirley functions, the green lines are the fitted peaks using Gaussian–Lorentzian sum functions, and the red line is the sum of fitted background and peaks.

material.[26−30] The fine scan of Fe 2p (Figure 5c) shows two main peaks (located at 711.0 and 724.9 eV), which can be assigned to Fe $2p_{3/2}$ and Fe $2p_{1/2}$, respectively. This is consistent with the XPS data of $ZnFe_2O_4$ reported in the literature,[28−32] confirming that all Fe ions in the $ZnFe_2O_4$ samples are in the +3 valence state. The existence of Fe in either 0 and +2 valence states can be excluded as significant chemical shift of either Fe^0 (with $2p_{3/2}$ at ∼707 eV) or Fe^{2+} (with $2p_{3/2}$ at ∼709 eV in oxides)[26] is absent. In addition, two satellite peaks are also observed around 718.9 and 733.3 eV, which are characteristic of the Fe^{3+} in the samples.[26,29−31] The fine scan of O 1s (Figure 5d) exhibits a two-peak feature, suggesting multiple origins of the O signals near sample surface. The peak located at 530.0 eV can be assigned to the lattice oxygen in $ZnFe_2O_4$ samples, while another peak at 531.5 eV comes from surface-adsorbed hydrocarbon.[26,28−30] Moreover, the atomic percentages of Zn, Fe, and O are also calculated after fitting the Zn, Fe, and O fine-scan spectra. The atomic ratio Zn:Fe:O of this sample is ∼1:2:4, suggesting stoichiometric $ZnFe_2O_4$.

Detailed Structure Study by EELS. EELS taken from three $ZnFe_2O_4$ nanotube samples calcinated at different temperatures (i.e., S400, S500, and S600) are then studied. The main features of O K edge energy loss spectra are also similar, showing four major peaks (A, B, C, and D), as described in the previous section (Figure 6a). However, by looking at peaks more closely (Figure 6b), one can see a subtle difference in the split peak A (labeled A1 and A2). Both the A1/A2 ratio and the separation between A1 and A2 vary with the calcination temperature. To make easy comparison, the spectra are normalized using peak A2 locating around 530.1 eV. The separation of A1 and A2 increases, while the relative intensity of A1 decreases when the calcination temperature increases from 400 to 600 °C.

The detailed comparisons of peak separations and ratios of A1/A2 are made by fitting the EELS spectra. Peaks A1 and A2 of three samples are fitted using Voigt functions,[22] and the corresponding results are shown in Figure 7. It is shown that when the calcination temperature increase from 400 to 600 °C,

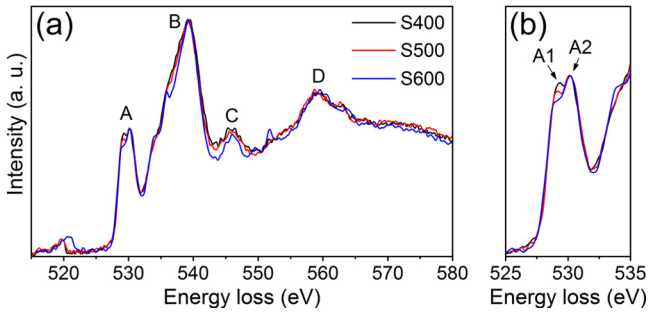

Figure 6. (a) O K edge energy loss spectra of sample S400 (black line), S500 (red line), and S600 (blue line), normalized with peak B locating around 539.2 eV. (b) Enlarged view of the same spectra in (a), normalized with peak A2 locating around 530.1 eV.

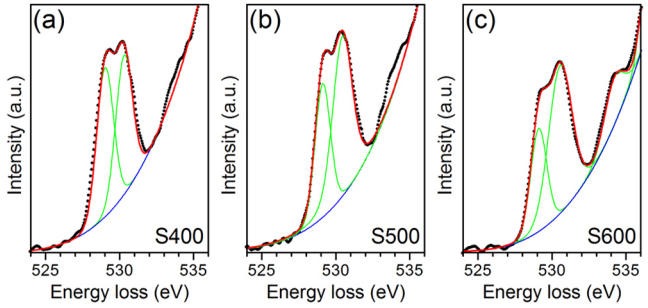

Figure 7. Peak fittings of A1 and A2 in the ELNES of sample (a) S400, (b) S500, and (c) S600, respectively. In each figure, the black dots are experimental ELNES data. The blue line, the green lines, and the red line are the fitted background, the fitted peaks, and their sum, respectively.

the separation of A1 and A2 increases from 1.26 to 1.45 eV and the relative intensity A1/A2 decreases from 1.07 to 0.70.

The change in peak separations of A1 and A2 and A1/A2 peak ratios relate to the change in the symmetry of O atoms around Fe^{3+} ions. More Fe^{3+} ions in A (tetrahedral) sites lead to larger A1/A2 ratios and smaller peak separations.[20,33−35] Therefore, sample S400 has largest amount of Fe^{3+} ions occupying A sites among the three samples. With the increase of the calcination temperature, more Fe^{3+} ions move from A sites to their equilibrium positions (B sites) and the crystal structure of the sample becomes closer to the normal spinel structure.

Magnetic Properties. The magnetic properties of the three stoichiometric nanotube samples S400, S500, and S600 were then studied in a systematic manner. The ZFC and FC curves (Figure 8a,c,e) of the three nanotube samples were measured under an external magnetic field of 50 Oe. In the tested temperature regions, every one of the ZFC curve shows a maximum (i.e., the blocking temperature, T_B). However, with the increase of the calcination temperature, T_B is shifted from 95 to 18 K (Table 2), while the corresponding magnetization is decreased.

The magnetic hysteresis loops of the three samples were also measured at both 3 and 300 K, which are well below and above the blocking temperatures of the samples (Figure 8b,d,f), respectively. The linear background of each magnetization curve has been subtracted. At 300 K, the sample S400 exhibits ferromagnetic behavior with the largest saturation magnetization (M_S) among the three (14 emu/g). With the calcination temperatures increasing from 400 to 600 °C, M_S of $ZnFe_2O_4$

dx.doi.org/10.1021/jp507991e | J. Phys. Chem. C 2014, 118, 30145−30152

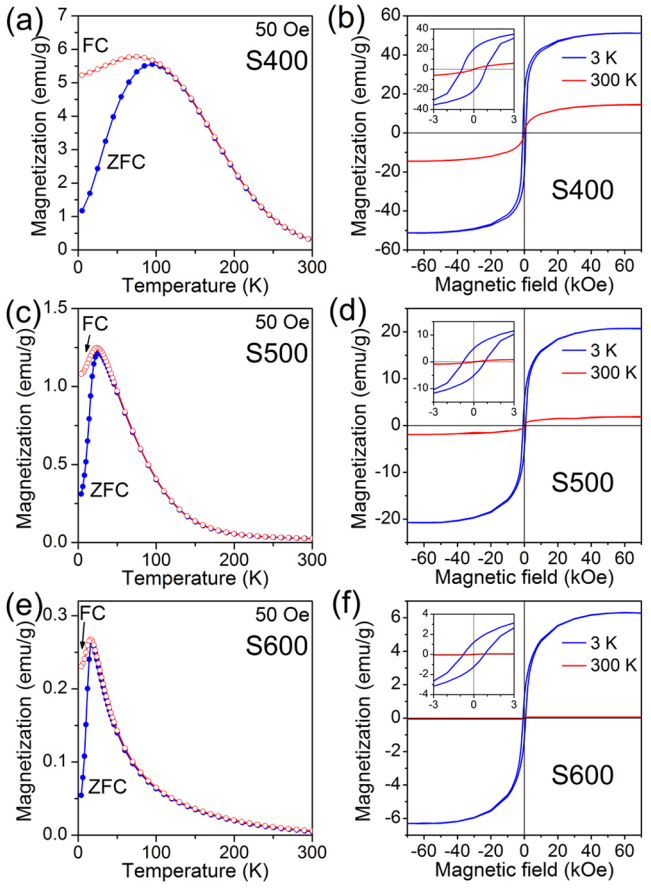

Figure 8. Zero-field-cooling (solid blue circle) and field-cooling (hollow red circle) curves of (a) sample S400, (c) S500, and (e) S600 under an external field of 50 Oe. Magnetization curves of (b) sample S400, (d) S500, and (f) S600 obtained at 3 K (blue line) and 300 K (red line), respectively. Inserts at top-left corner of panels a, c, and e show the magnified views of the corresponding magnetization curves.

Table 2. Summary of Magnetic Properties of Samples S400, S500, and S600

sample	T_B (K)	M_S at 3 K (emu/g)	M_S at 300 K (emu/g)	H_C at 3 K (Oe)	H_C at 300 K (Oe)
S400	95	51	14	885	<50
S500	26	21	1.9	810	
S600	18	6.3	0.062	790	

nanotubes dramatically drops from 14 to 0.062 emu/g. On the other hand, the coercivities (H_C) of all three samples are small at 300 K (<50 Oe).

When being cooled down to 3 K, the M_S value of S400 increases to 51 emu/g and H_C reaches 885 Oe, both of which are the largest among the three samples. When increasing the calcination temperatures from 400 to 600 °C, M_S at 3 K show a near-1-order-of-magnitude decrease from 51 to 6.3 emu/g. Nonetheless, H_C only slightly decrease from 885 to 790 Oe. The variations of the magnetic properties of S400, S500, and S600 are summarized in Table 2.

In principle, the ideal $ZnFe_2O_4$ has the normal spinel structure with all the Zn^{2+} occupying A sites and Fe^{3+} occupying B sites. It is antiferromagnetic, showing linear magnetization curve without saturation. Its ZFC/FC curve presents a cusp at Néel temperature (~10 K).[1] However, magnetic properties (e.g., T_B, M_S, etc.) of the $ZnFe_2O_4$ in the present sample series (i.e., S400, S500, and S600) deviate from the ideal one, suggesting cation inversion to different extent from S400 to S600. In fact, as evidenced by the corresponding ELNES of O K edges, more Fe^{3+} ions migrate from the equilibrium B sites to A sites and more Zn^{2+} ions move from the equilibrium A sites to B sites (i.e., larger degree of cation inversion) when the calcination temperature decreases from 600 to 400 °C.

The cation inversion in $ZnFe_2O_4$ leads to the A−O−A and A−O−B superexchange interactions between the Fe^{3+} cations. The strength of the superexchange interaction depends on the angle and distances between metal−O−metal. In $ZnFe_2O_4$, A−O−B superexchange is the strongest and A−O−A superexchange is the weakest.[10] Hence, the ferromagnetism and large values of M_S mainly originate from the A−O−B superexchange interactions. Such interaction does not exist in normal spinel $ZnFe_2O_4$ because all Fe^{3+} are located in B sites, resulting in B−O−B antiferromagnetic coupling. The drastic drop of M_S of the samples prepared at higher calcination temperatures is probably attributed to the redistribution of Zn^{2+} and Fe^{3+} ions toward the normal spinel structure (i.e., fewer Fe^{3+} ions at A sites), and then the magnetic interactions between the Fe^{3+}cations in the A sites and B sites are weakened, and antiparallel coupling between the Fe^{3+} ions in the B sites becomes dominant.

In addition, the existence of the cation inversion causes the shift of ZFC/FC maxima (i.e., T_B) to higher temperatures compared to that of the ideal $ZnFe_2O_4$ (i.e., T_N for antiferromagnetic $ZnFe_2O_4$, ~10 K).[13,15,36] This can be explained by the larger degree of cation inversion of the sample synthesized at lower temperatures, resulting in larger magnetic anisotropy (i.e., larger K).[37,38]

Beside the redistribution of Fe and Zn ions in $ZnFe_2O_4$, the size effect has also been proposed as the origins of the ferromagnetism of $ZnFe_2O_4$ nanoparticles.[38] It is suggested that for very small $ZnFe_2O_4$ (in the range of a few nanometers) nanoparticles the effect of unbalanced spins on the surface becomes dominant, leading to the ferromagnetic behavior of nanosized $ZnFe_2O_4$. As revealed by XRD and TEM data, the crystalline size is in the range of a few tens of nanometers and the size distribution of all $ZnFe_2O_4$ samples are rather similar (23−28 nm); thus, the size effect should not be the main reason responsible for the large difference in the magnetic behaviors of the samples.

Stoichiometry Effect on $ZnFe_2O_4$ Nanotubes. In this series of samples, we maintained the calcination temperature at 500 °C, while the Fe:Zn ratios in $ZnFe_2O_4$ nanotubes are manipulated, so that sample S500 has stoichiometry chemical composition, and S500NS is associated with Fe:Zn ratio greater than 2.

As shown in Figure 9a, the survey scan of XPS spectrum collected from the nonstoichiometric sample S500NS also shows signals of Zn, Fe, and O only, being the same as the stoichiometric samples, although the Zn 2p peaks become relatively weaker. The fine scans of Zn 2p, Fe 2p, and O 1s (Figure 9b−d) also present similar peak positions and shapes comparing to those of the stoichiometric sample, indicating that the oxidation states of Zn and Fe are +2 and +3, respectively. Furthermore, the calculated atomic percentages of Zn, Fe, and O are 11.3, 30.8, and 57.9, and the Zn:Fe:O ratio is ~1:2.7:5.1, deriving from the stoichiometric ratio 1:2:4.

Detailed Structure Study by EELS. The O K edge energy loss spectrum of S500NS is then collected, showing a similar four-peak feature to that of S500 (Figure 10). However, the

dx.doi.org/10.1021/jp507991e | J. Phys. Chem. C 2014, 118, 30145−30152

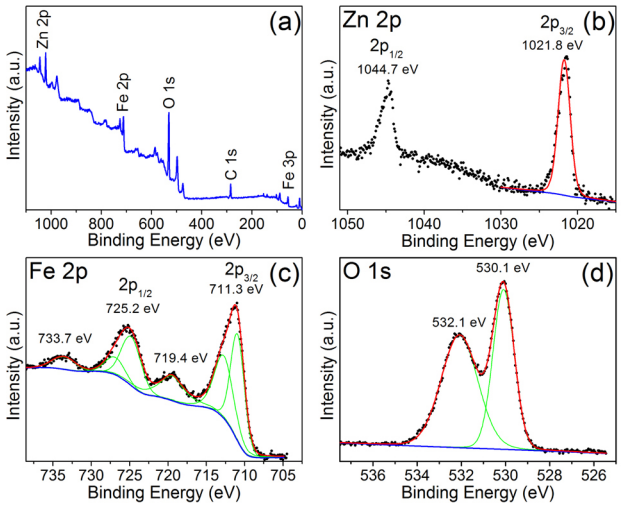

Figure 9. XPS spectrum of (a) survey scan and fine scans (black dots) of (b) Zn 2p, (c) Fe 2p, and (d) O 1s taken from the nonstoichiometric $ZnFe_2O_4$ nanotube sample S500NS. In panels b–d, the blue line is the fitted background using Shirley functions, the green lines are the fitted peaks using Gaussian–Lorentzian sum functions, and the red line is the sum of fitted background and peaks.

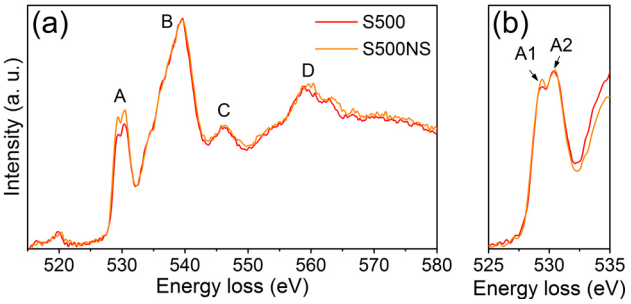

Figure 10. (a) O K edge energy loss spectra of sample S500 (red line) and S500NS (orange line), normalized with the peak locating around 539.2 eV. (b) Enlarged view of the same spectra in (a), normalized with the peak locating around 530.1 eV.

peak ratio B/A in the spectrum of S500NS is larger than that of S500, which is probably due to existence of extra Fe^{3+} ions in the nonstoichiometric sample. Using the same curve fitting procedures described above, the ELNES of S500NS is also fitted. The peak separation and intensity ratio of A1 and A2 of S500NS (1.32 eV and 0.91) are both similar to those of S500 (1.30 eV and 0.89), as shown in Figure 11. This indicates the ratios between Fe^{3+} ions occupying in A sites and B sites in the nonstoichiometric sample is close to that of the stoichiometric sample.

Magnetic Properties. The magnetic properties of the nonstoichiometric sample S500NS were then studied and compared with the corresponding stoichiometric sample S500. As shown in Figure 12c, T_B of S500NS is shifted to 125 K, being significantly higher comparing to that of S500 (i.e., 26 K). Figure 12d shows larger M_S of the nonstoichiometric sample (28 and 12 emu/g) than those of the stoichiometric ones (21 and 1.9 emu/g) at both 3 and 300 K, with more obvious difference observed at 300 K. Furthermore, the coercivity (H_C) of S500NS (1036 Oe) is also larger than that of S500 (810 Oe). The comparisons of the magnetic properties of S500 and S500NS are summarized in Table 3.

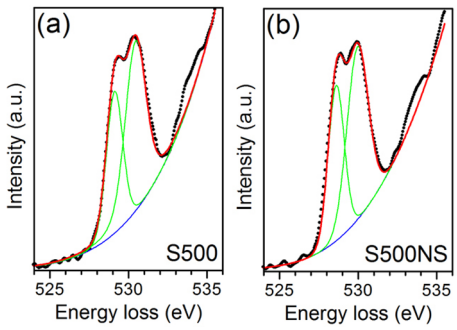

Figure 11. (a, b) Peak fittings of A1 and A2 in the ELNES of sample S500 and S500NS, respectively. In each figure, the black dots are experimental ELNES data. The blue line, the green lines, and the red line are the fitted background, the fitted peaks, and their sum, respectively.

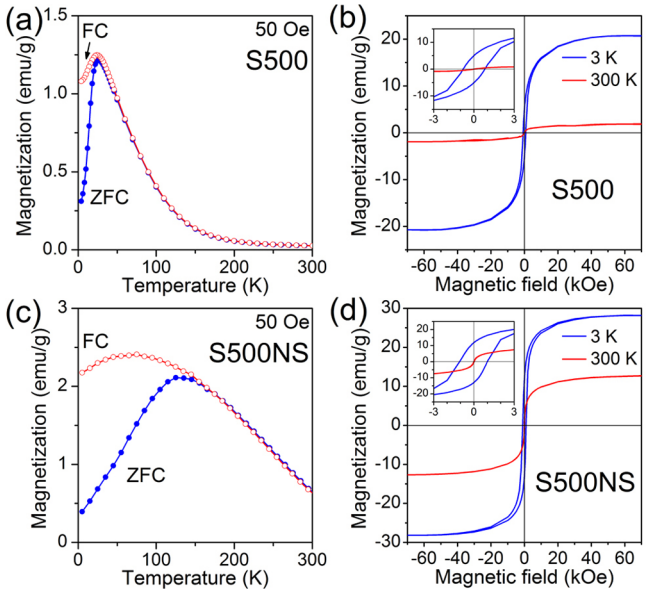

Figure 12. Zero-field-cooling (solid blue circle) and field-cooling (hollow red circle) curves of (a) sample S500 and (c) S500NS under an external field of 50 Oe. Magnetization curves of (b) sample S500 and (d) S500NS obtained at 3 K (blue line) and 300 K (red line), respectively. Insets at top-left corner of (a) and (c) show the magnified views of the corresponding magnetization curves.

Table 3. Brief Summary of Magnetic Properties of Samples S500 and S500NS

sample	T_B (K)	M_S at 3 K (emu/g)	M_S at 300 K (emu/g)	H_C at 3 K (Oe)	H_C at 300 K (Oe)
S500	26	21	1.9	810	<50
S500NS	125	28	12	1036	

The O K edge ELNES of the nonstoichiometric sample S500NS suggests that the Fe^{3+} ions in the structure occupying both A sites and B sites with similar ratio of the corresponding stoichiometric sample S500. Then the increase in T_B, magnetic anisotropy constant K, and M_S in S500NS comparing to those of S500[5,7] must be resulted from the extra Fe^{3+} ions, which introduce additional unbalanced spins in the structure.

CONCLUSIONS

The fine structures of O K edge electron energy loss spectroscopy taken from $ZnFe_2O_4$ nanotubes (i.e., the splitting

dx.doi.org/10.1021/jp507991e | J. Phys. Chem. C 2014, 118, 30145–30152

of peak A) change with the calcination temperature, but not the chemical composition. Such subtle changes in the O K edge fine structure suggest that Fe^{3+} migrate from their equilibrium positions (octahedral B sites) to the tetrahedral A sites, causing deviation from the normal spinel structure of $ZnFe_2O_4$. This results in enhanced superexchange interactions of Fe^{3+} ions and thus leads to different magnetic properties (ferromagnetic vs antiferromagnetic in normal spinel structure). Although nonstoichiometric $ZnFe_2O_4$ nanotube samples show a different magnetic behavior as compared to the stoichiometric ones, this is resulted from the extra Fe^{3+} ions in the lattice, but not related to cation A−B site reversion. This is suggested by the similar feature of peak A splitting obtained from the corresponding nonstoichiometric and stoichiometric samples.

AUTHOR INFORMATION

Corresponding Author

*E-mail liquan@phy.cuhk.edu.hk; Tel +852 39436323 (Q.L.).

Author Contributions

Xuan Guo, Haojun Zhu, and Quan Li conceived and designed the experiments, analyzed the data, and cowrote the paper. Xuan Guo and Haojun Zhu synthesized the materials and performed basic characterizations. Mingsu Si, Changjun Jiang, and Desheng Xue performed the magnetic characterizations. Zhihua Zhang discussed the interpretation of the EELS results.

Notes

The authors declare no competing financial interest.

ACKNOWLEDGMENTS

This work is supported by UGC under project No. SEG_CUHK06 and National Basic Research Program of China (Grant No. 2012CB933101).

REFERENCES

(1) Mathew, D. S.; Juang, R. S. An Overview of the Structure and Magnetism of Spinel Ferrite Nanoparticles and Their Synthesis in Microemulsions. *Chem. Eng. J.* **2007**, *129*, 51−65.

(2) Hamdeh, H. H.; Ho, J. C.; Oliver, S. A.; Willey, R. J.; Oliveri, G.; Busca, G. Magnetic Properties of Partially-Inverted Zinc Ferrite Aerogel Powders. *J. Appl. Phys.* **1997**, *81*, 1851−1857.

(3) Goya, G. F.; Rechenberg, H. R. Ionic Disorder and Neel Temperature in $ZnFe_2O_4$ Nanoparticles. *J. Magn. Magn. Mater.* **1999**, *196*−*197*, 191−192.

(4) Burghart, F.; Potzel, W.; Kalvius, G.; Schreier, E.; Grosse, G.; Noakes, D.; Schäfer, W.; Kockelmann, W.; Campbell, S.; Kaczmarek, W. Magnetism of Crystalline and Nanostructured $ZnFe_2O_4$. *Physica B* **2000**, *289*, 286−290.

(5) Hochepied, J. F.; Bonville, P.; Pileni, M. P. Nonstoichiometric Zinc Ferrite Nanocrystals: Syntheses and Unusual Magnetic Properties. *J. Phys. Chem. B* **2000**, *104*, 905−912.

(6) Chinnasamy, C. N.; Narayanasamy, A.; Ponpandian, N.; Chattopadhyay, K. The Influence of Fe^{3+} Ions at Tetrahedral Sites on the Magnetic Properties of Nanocrystalline $ZnFe_2O_4$. *Mater. Sci. Eng., A* **2001**, *304*, 983−987.

(7) Grasset, F.; Labhsetwar, N.; Li, D.; Park, D. C.; Saito, N.; Haneda, H.; Cador, O.; Roisnel, T.; Mornet, S.; Duguet, E.; et al. Synthesis and Magnetic Characterization of Zinc Ferrite Nanoparticles with Different Environments: Powder, Colloidal Solution, and Zinc Ferrite-silica Core-shell Nanoparticles. *Langmuir* **2002**, *18*, 8209−8216.

(8) Ehrhardt, H.; Campbell, S. J.; Hofmann, M. Magnetism of the Nanostructured Spinel Zinc Ferrite. *Scr. Mater.* **2003**, *48*, 1141−1146.

(9) Hofmann, M.; Campbell, S. J.; Ehrhardt, H.; Feyerherm, R. The Magnetic Behaviour of Nanostructured Zinc Ferrite. *J. Mater. Sci.* **2004**, *39*, 5057−5065.

(10) Li, F. S.; Wang, L.; Wang, J. B.; Zhou, Q. G.; Zhou, X. Z.; Kunkel, H. P.; Williams, G. Site Preference of Fe in Nanoparticles of $ZnFe_2O_4$. *J. Magn. Magn. Mater.* **2004**, *268*, 332−339.

(11) Sepelak, V.; Becker, K. D. Comparison of the Cation Inversion Parameter of the Nanoscale Milled Spinel Ferrites with that of the Quenched Bulk Materials. *Mater. Sci. Eng., A* **2004**, *375*, 861−864.

(12) Atif, M.; Hasanain, S. K.; Nadeem, M. Magnetization of Sol-Gel Prepared Zinc Ferrite Nanoparticles: Effects of Inversion and Particle Size. *Solid State Commun.* **2006**, *138*, 416−421.

(13) Nakashima, S.; Fujita, K.; Tanaka, K.; Hirao, K.; Yamamoto, T.; Tanaka, I. First-Principles XANES Simulations of Spinel Zinc Ferrite with a Disordered Cation Distribution. *Phys. Rev. B* **2007**, *75*, 174443.

(14) Stewart, S. J.; Figueroa, S. J. A.; Lopez, J. M.; Marchetti, S. G.; Bengoa, J. F.; Prado, R. J.; Requejo, F. G. Cationic Exchange in Nanosized $ZnFe_2O_4$ Spinel Revealed by Experimental and Simulated Near-Edge Absorption Structure. *Phys. Rev. B* **2007**, *75*, 073408.

(15) Upadhyay, C.; Verma, H. C.; Sathe, V.; Pimpale, A. V. Effect of Size and Synthesis Route on the Magnetic Properties of Chemically Prepared Nanosize $ZnFe_2O_4$. *J. Magn. Magn. Mater.* **2007**, *312*, 271−279.

(16) Akhtar, M. J.; Nadeem, M.; Javaid, S.; Atif, M. Cation Distribution in Nanocrystalline $ZnFe_2O_4$ Investigated Using X-ray Absorption Fine Structure Spectroscopy. *J. Phys.: Condens. Matter* **2009**, *21*, 405303.

(17) Ayyappan, S.; Raja, S. P.; Venkateswaran, C.; Philip, J.; Raj, B. Room Temperature Ferromagnetism in Vacuum Annealed $ZnFe_2O_4$ Nanoparticles. *Appl. Phys. Lett.* **2010**, *96*, 143106.

(18) Tanaka, K.; Makita, M.; Shimizugawa, Y.; Hirao, K.; Soga, N. Structure and High Magnetization of Rapidly Quenched Zinc Ferrite. *J. Phys. Chem. Solids* **1998**, *59*, 1611−1618.

(19) Schiessl, W.; Potzel, W.; Karzel, H.; Steiner, M.; Kalvius, G. M.; Martin, A.; Krause, M. K.; Halevy, I.; Gal, J.; Schafer, W.; et al. Magnetic Properties of the $ZnFe_2O_4$ Spinel. *Phys. Rev. B* **1996**, *53*, 9143−9152.

(20) Colliex, C.; Manoubi, T.; Ortiz, C. Electron-Energy-Loss-Spectroscopy Near-Edge Fine Structures in the Iron-Oxygen System. *Phys. Rev. B* **1991**, *44*, 11402−11411.

(21) Guo, X.; Zhu, H.; Si, M.; Jiang, C.; Xue, D.; Li, Q. Tuning the Composition of Zn-Fe-O Nanotube Arrays: from Zinc Ferrite $ZnFe_2O_4$ to Hematite α-Fe_2O_3. *CrystEngComm* **2013**, *15*, 8306−8313.

(22) Wertheim, G. K.; Butler, M. A.; West, K. W.; Buchanan, D. N. E. Determination of the Gaussian and Lorentzian Content of Experimental Line Shapes. *Rev. Sci. Instrum.* **1974**, *45*, 1369−1371.

(23) Maletin, M.; Moshopoulou, E. G.; Kontos, A. G.; Devlin, E.; Delimitis, A.; Zaspalis, V.; Nalbandian, L.; Srdic, V. V. Synthesis and Structural Characterization of In-doped $ZnFe_2O_4$ Nanoparticles. *J. Eur. Ceram. Soc.* **2007**, *27*, 4391−4394.

(24) Bo, X. X.; Li, G. S.; Qiu, X. Q.; Xue, Y. F.; Li, L. P. Magnetic Diphase Nanostructure of $ZnFe_2O_4$/gamma-Fe_2O_3. *J. Solid State Chem.* **2007**, *180*, 1038−1044.

(25) Williams, D. B.; Carter, C. B. *Transmission Electron Microscopy: a Textbook for Materials Science*; Springer: Berlin, 1996.

(26) Moulder, J. F.; Stickle, W. F.; Sobol, P. E.; Bomben, K. D. *Handbook of X-ray Photoelectron Spectroscopy: a Reference Book of Standard Spectra for Identification and Interpretation of XPS Data*; Perkin-Elmer Corporation, Physical Electronics Division: Eden Prairie, MN, 1992.

(27) Li, X.; Hou, Y.; Zhao, Q.; Teng, W.; Hu, X.; Chen, G. Capability of Novel $ZnFe_2O_4$ Nanotube Arrays for Visible-Light Induced Degradation of 4-Chlorophenol. *Chemosphere* **2010**, *82*, 581−586.

(28) Hou, Y.; Li, X. Y.; Zhao, Q. D.; Quan, X.; Chen, G. H. Electrochemical Method for Synthesis of a $ZnFe_2O_4$/TiO_2 Composite Nanotube Array Modified Electrode with Enhanced Photoelectrochemical Activity. *Adv. Funct. Mater.* **2010**, *20*, 2165−2174.

(29) Sharma, Y.; Sharma, N.; Rao, G. V. S.; Chowdari, B. V. R. Li-storage and Cyclability of Urea Combustion Derived $ZnFe_2O_4$ as Anode for Li-ion Batteries. *Electrochim. Acta* **2008**, *53*, 2380−2385.

(30) Lv, H. J.; Ma, L.; Zeng, P.; Ke, D. N.; Peng, T. Y. Synthesis of Floriated $ZnFe_2O_4$ with Porous Nanorod Structures and Its Photo-

catalytic Hydrogen Production under Visible Light. *J. Mater. Chem.* **2010**, *20*, 3665−3672.
(31) Wang, M.; Ai, Z. H.; Zhang, L. Z. Generalized Preparation of Porous Nanocrystalline $ZnFe_2O_4$ Superstructures from Zinc Ferrioxalate Precursor and Its Superparamagnetic Property. *J. Phys. Chem. C* **2008**, *112*, 13163−13170.
(32) Hou, Y.; Li, X. Y.; Zhao, Q. D.; Quan, X.; Chen, G. H. Electrochemically Assisted Photocatalytic Degradation of 4-Chlorophenol by $ZnFe_2O_4$-Modified TiO_2 Nanotube Array Electrode under Visible Light Irradiation. *Environ. Sci. Technol.* **2010**, *44*, 5098−5103.
(33) Paterson, J. H. ELNES of 3d Transition-metal Oxides: II. Variations with Oxidation State and Crystal Structure. *Ultramicroscopy* **1990**, *32*, 319−325.
(34) Jin, C.; Li, P.; Mi, W.; Bai, H. Structure, Magnetic, and Transport Properties of Epitaxial $ZnFe_2O_4$ Films: an Experimental and First-Principles Study. *J. Appl. Phys.* **2014**, *115*, 213908.
(35) Soliman, S.; Elfalaky, A.; Fecher, G. H.; Felser, C. Electronic Structure Calculations for $ZnFe_2O_4$. *Phys. Rev. B* **2011**, *83*, 085205.
(36) Yao, C. W.; Zeng, Q. S.; Goya, G. F.; Torres, T.; Liu, J. F.; Wu, H. P.; Ge, M. Y.; Zeng, Y. W.; Wang, Y. W.; Jiang, J. Z. $ZnFe_2O_4$ Nanocrystals: Synthesis and Magnetic Properties. *J. Phys. Chem. C* **2007**, *111*, 12274−12278.
(37) Bullita, S.; Casu, A.; Casula, M. F.; Congiu, F.; Concas, G.; Corrias, A.; Falqui, A.; Loche, D.; Marras, C. $ZnFe_2O_4$ Nanoparticles Dispersed in a Highly Porous Silica Aerogel Matrix: a Magnetic Study. *Phys. Chem. Chem. Phys.* **2014**, in press.
(38) Blanco-Gutiérrez, V.; Torralvo-Fernandez, M. J.; Sáez-Puche, R. Magnetic Behavior of $ZnFe_2O_4$ Nanoparticles: Effects of a Solid Matrix and the Particle Size. *J. Phys. Chem. C* **2010**, *114*, 1789−1795.